journal of the mechanical behavior of biomedical materials 155 (2024) 106555

Contents lists available at ScienceDirect

Journal of the Mechanical Behavior of Biomedical Materials

journal homepage: www.elsevier.com/locate/jmbbm

# 3D-printed bioinspired spicules: Strengthening and toughening via stereolithography

Fariborz Tavangarian [a,b,*], Sorour Sadeghzade [a,c], Niloofar Fani [a], Dariush Khezrimotlagh [d], Keivan Davami [e]

[a] Mechanical Engineering Program, School of Science, Engineering and Technology, Penn State Harrisburg, Middletown, PA, 17057, United States
[b] Department of Biomedical Engineering, Pennsylvania State University, University Park, State College, PA, 16802, United States
[c] Shenzhen Key Laboratory of Soft Mechanics & Smart Manufacturing, Department of Mechanics and Aerospace Engineering, Southern University of Science and Technology, Shenzhen, 518055, China
[d] Mathematical Sciences Program, School of Science, Engineering and Technology, Penn State Harrisburg, Middletown, PA, 17057, United States
[e] Department of Mechanical Engineering, University of Alabama, Tuscaloosa, AL, 35487, United States

ARTICLE INFO

*Keywords:*
Lightweight materials
Biomimetic structures
Rigid resin
Spicule-inspired structure
Stereolithography
Euplectella aspergillum sponge

ABSTRACT

Recently, the replication of biological microstructures has garnered significant attention due to their superior flexural strength and toughness, coupled with lightweight structures. Among the most intriguing biological microstructures renowned for their flexural strength are those found in the Euplectella Aspergillum (EA) marine sponges. The remarkable strength of this sponge is attributed to its complex microstructure, which consists of concentric cylindrical layers known as spicules with organic interlayers. These features effectively impede large crack propagation, imparting extraordinary mechanical properties. However, there have been limited studies aimed at mimicking the spicule microstructure. In this study, structures inspired by spicules were designed and fabricated using the stereolithography (SLA) 3D printing technique. The mechanical properties of concentric cylindrical structures (CCSs) inspired by the spicule microstructure were evaluated, considering factors such as the wall thickness of the cylinders, the number of layers, and core diameter, all of which significantly affect the mechanical response. These results were compared with those obtained from solid rods used as solid samples. The findings indicated that CCSs with five layers or fewer exhibited a flexural strength close to or higher than that of solid rods. Particularly, samples with 4 and 5 cylindrical layers displayed architecture similar to natural spicules. Moreover, in all CCSs, the absorbed energy was at least 3–4 times higher than solid rods. Conversely, CCSs with a cylinder wall thickness of 0.65 mm exhibited a more brittle behavior under the 3-point bending test than those with 0.35 mm and 0.5 mm wall thicknesses. CCSs demonstrated greater resistance to failure, displaying different crack propagation patterns and shear stress distributions under the bending test compared to solid rods. These results underscore that replicating the structure of spicules and producing structures with concentric cylindrical layers can transform a brittle structure into a more flexible one, particularly in load-bearing applications.

## 1. Introduction

Producing lightweight materials and structures with excellent strength and toughness for aerospace, energy harvesting, transportation, automobile, construction, and biomedical applications has received significant attention (Das, 2001; Joshi and Chatterjee, 2016; Yancey, 2016). To this end, nature inspires scientists to solve human problems and design structures with exceptional properties (Luz and Mano, 2009; Sun and Bhushan, 2012). Highly mineralized biological structures, such as tooth enamel, nacre, bone, and crustacean exoskeletons, possess intricate structures (Barthelat, 2023; Zhou et al., 2023). These structures comprise organized arrangements of inorganic mineral components within an organic matrix (Jin et al., 2020). The precise architecture of these biological structures contributes to their exceptional mechanical properties, including strength, hardness, and toughness (Zhao et al., 2022a, 2022b).

* Corresponding author. Mechanical Engineering Program, School of Science, Engineering and Technology, Penn State Harrisburg, Middletown, PA, 17057, United States.
*E-mail addresses:* f.tavangarian@gmail.com, fut16@psu.edu (F. Tavangarian).

https://doi.org/10.1016/j.jmbbm.2024.106555
Received 19 February 2024; Received in revised form 8 April 2024; Accepted 15 April 2024
Available online 17 April 2024

Euplectella aspergillum (EA) marine sponge (known as the biological glass structure) (Minchin, 1909; Tang et al., 2019) is another attractive mineralized biological structure that has received significant attention and exhibits a remarkable and intricate microstructure which called spicule (Saito et al., 2002). This spicule structure is crucial in providing the organism with structural support and mechanical strength (Wang et al., 2012). As shown in Fig. 1a, spicules in EA are composed of hydrated silica and are arranged in a lattice-like structure, forming a cylindrical mesh-like framework (Fig. 1a–d) with protein as an interlayer (Fig. 1f–i) (Uriz et al., 2003).

Previous studies have shown that the natural spicule exhibits a distinctive "sawtooth" pattern. This pattern suggests that the spicules can undergo stable crack propagation and highly resist damage, unlike traditional silica rods that fail catastrophically (Mayer et al., 2004; Sarikaya et al., 2001). Therefore, mimicking the microstructure of the spicule can be a promising approach to achieving remarkable mechanical properties in materials with inherent brittleness.

Recently, some researchers have tried to mimic this structure. For instance researcher printed the skeletal lattice of EA. They focused on understanding the skeletal lattice's design principles and architecture. Using this knowledge to develop accurate finite element (FE) models and manufactured a scaled engineering analog using 3D additive manufacturing (AM) (Adibeig et al., 2023; Hassanifard et al., 2022). While the printed specimens exhibited failure patterns similar to those of the biological system, the specific microstructural features of the spicules were not directly mimicked in the engineering reproduction (Robson Brown et al., 2019). In another study Yang et al. (2022) created flexible brushite/sodium alginate scaffolds using 3D printing, incorporating spicule-like microstructures. While claiming resemblance to natural spicules, their scaffolds had a brick-mortar structure similar to nacre, differing from silica layers in natural spicules. Despite this, their 3D printing technique offers notable advantages for complex structure fabrication (Mirkhalaf et al., 2023; Wei et al., 2023; Zhou et al., 2023). Among all 3D-printing techniques for polymers, the SLA approach has

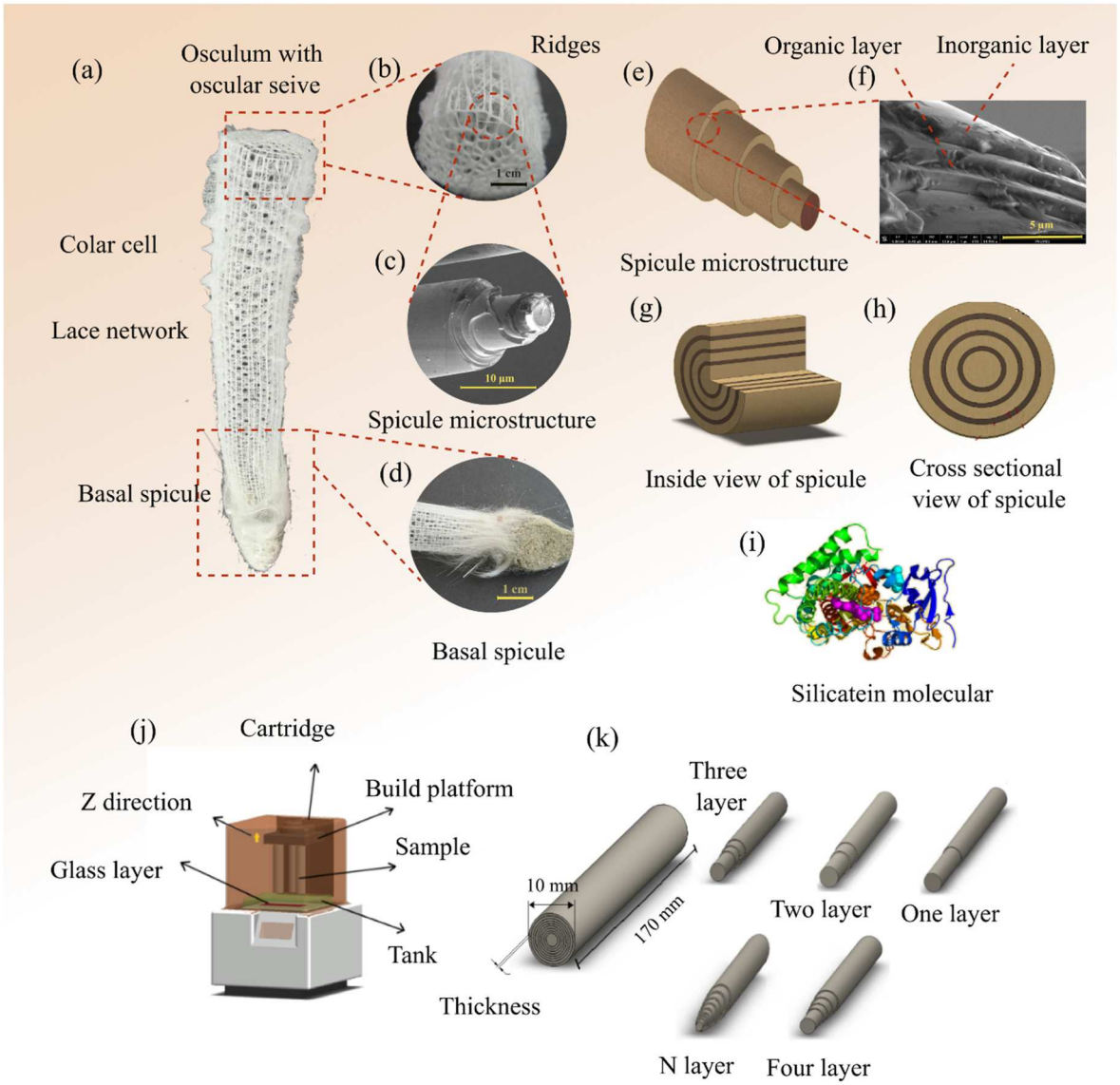


**Fig. 1.** (a–d) Skeleton of Euplectella Aspergillum (EA), (e) Schematic of spicule structure, (f) SEM image of spicule structure showing the alternating concentric cylindrical layers of hydrated silica, (g) Schematic inside view of spicule structure, (h) Cross sectional view of spicule structure and (i) Silicatin polymer molecules as organic layers between the silica cylinders, (j) Designing the 3D model and fabrication procedure of spicule-inspired structure (CCSs) as well as solid rods (CS) with stereolithography (SLA) technique, (k) Schematic representation of the assembling procedure of spicule-inspired structures with different number of layers and thicknesses.

demonstrated a better feasibility regarding building devices' high rate, accuracy, and quality (Wang et al., 2016). In our previous studies (Sadeghzade et al., 2020a; Tavangarian et al., 2021), we developed spicule-inspired structures with improved mechanical properties to some extent. Two methods have been used to print the samples. In the first technique, spicule-inspired structures were printed simultaneously. We used an innovatively simultaneous printing approach, enabling the creation of a unified structure with concentric cylindrical layers. This new method optimizes the integration of the layers, promoting better bonding and overall structural integrity. Also, we considered various interlayer spacings, acknowledging the pivotal role of these spaces in maintaining structural integrity and stress distribution. We found that at least 550 μm inter-cylinder spacing is required to print discrete consecutive cylindrical layers, adversely affecting the specimens' efficiency and performance (Sadeghzade et al., 2020a). Furthermore, previously, we investigated a range of layer thicknesses, pushing the limits of the Form 2 printer's capabilities to achieve thicknesses more closely aligned with those found in natural spicule structures. Layer thickness represents a critical parameter that significantly influences the structural integrity and ultimate mechanical properties of Spicule-Inspired Structures (SISs).

As mentioned before, the spicule structure (as shown in Fig. 1c), characterized by a central core surrounded by multiple layers, plays a crucial role in both biological function and mechanical performance. The core significantly influences the mechanical properties of the spicule, providing structural integrity and stability. Furthermore, the number and arrangement of layers around the core contribute to the spicule's strength, flexibility, and efficiency in performing mechanical functions. By considering these parameters in the design process, we have developed a new design of spicule-inspired structures that achieves specific functional objectives in current study. Building upon previous studies, this research offers a comprehensive analysis of multiple design parameters affecting the mechanical performance of these structures, including the core diameter. This examination allows for a deeper understanding of the interactions between design variables and provides insights into optimizing spicule-inspired structures for various applications. Therefore, in our current study, we continue to explore various layer thicknesses, recognizing their potential impact on the mechanical performance of CCSs. In each group of samples, cylinders were printed separately with similar wall thickness and different diameters and then inserted into each other. In our previous study, we printed and tested layers with various diameters and consistent wall thicknesses to assess the performance of spicule-inspired structures. However, we did not explore the impact of gradually reducing the diameter of the initial solid core while increasing the number of layers surrounding it (Tavangarian et al., 2021). This will offer valuable insights on how the mechanical properties of spicule-inspired structures are influenced by adding more layers around a solid core. As a result, in this study the influence of thickness, number of the cylindrical layers and the size of solid core in CCSs on the mechanical properties of the samples were evaluated. For this purpose, to understand the relation between the number of layers and core size with the flexural strength, strain, modulus, and absorbed energy of the final samples, the CCSs with 2-, 3-, 4-, …, N-layers (depending on the selected thickness) were printed. Also, CCSs' stress distribution and crack propagation were studied and compared with the solid rods.

## 2. Materials and methods

### 2.1. Microstructure characterization of natural and spicule-inspired structures

Scanning electron microscope (SEM, Helios Nanolab 660 with an acceleration voltage of 20 kV) was utilized to evaluate the microstructure and fracture surface of natural spicules to design the inspired spicule structure. For this purpose, the spicules were first washed with hydrogen peroxide and subsequently rinsed with distilled water to remove any tissue, as described in (Murr, 2006). The cleaned spicules were dried in an oven at 60 °C for 24 h. Finally, the samples were coated with iridium to prevent surface charges under the microscope. The crack propagation patterns and toughening mechanism of CCSs on the macro and micro scales were evaluated with the aid of an optical microscope (Smartzoom5, Digital microscope, Carl-Zeissss-Promenade 10, Germany) and Scanning electron microscope (SEM, Helios Nanolab 660, acceleration voltage of 30 kV)

### 2.2. Fabrication of concentric cylindrical structures (CCSs) with core

A 3D printing technique using stereolithography (SLA) was utilized to fabricate the samples with concentric cylindrical structures (CCSs). This method allowed us to precisely fabricate the cylindrical as well as solid rods, enabling the creation of complex structures with high accuracy and resolution. A schematic representation of *Form 2* (3D printer) with an SLA method is demonstrated in Fig. 1j. A polymer-based resin (*Rigid Resin*, RR, purchased from *Formlab* company) was used to print the CCSs and solid samples (as solidsolid samples). RR is reinforced with glass to offer high stiffness and a polished surface. This material is highly deformation-resistant over time and is great for printing thin walls and features. This type of resin shows brittle behavior. Also, it has the highest modulus (flexural modulus of 3.7 GPa and tensile modulus of 4.1 GPa) of all *Formmlab*'s materials with great heat resistance and stability. This resin enabled us to achieve the desired mechanical characteristics and structural integrity in the fabricated CCSs. CCSs and solid samples were printed by converting liquid photopolymers, one layer at a time. The parameter settings of *the Form 2* printer were shown in Table 1. The fabrication procedure of CCS samples with core was presented in Fig. 1k. Cylinders with different thicknesses (0.35, 0.5, and 0.65 mm) and diameters, including solid cores, were designed in SolidWorks software and the STL files were sent to *Preform* software for printing.

As can be seen in Fig. 1k, the design of the samples was made up of a core and several cylindrical layers around the cores. The cylinders and cores were inserted into each other. In order to determine the effect of the number of layers and core size on the mechanical properties and the failure mechanism, the number of outer layers was chosen from one to the extent that the resolution of *the Form 2* printer allowed. The maximum number of layers for samples with different thicknesses of 0.35, 0.5, and 0.65 mm was limited to 9, 7, and 5, respectively, excluding the solid core. This limitation was imposed by the printer resolution, which prevented the printing of additional layers. Also, the outer diameter and height of all CCSs and solid samples were kept constant at 10 and 170 mm, respectively, based on the ASTM D790-15 standard for bending test ("Flexural Strength of Ceramic and Glass Rods," n.d.; Monn and Kesari, 2017) and 3D printer capability to print the maximum length. The designation and details of all samples were described in Table 2. After printing, all the samples were sonicated with isopropanol alcohol 99% for 20 min and then cured at 60 °C under UV light for 30 min.

### 2.3. Mechanical and physical properties characterization

We utilized the 3-point bending test for all the sample to assess its mechanical behavior under bending stress. Given the spicule's cylindrical shape and intended function as a support structure, the 3-point bending test offers a suitable method to measure its mechanical properties and assess its performance in practical applications. The mechanical properties were tested with MTS Insight (Electromechanical 30 kN Standard Length). The flexural stress, strain, and modules were calculated according to equations (1)–(3), respectively (Gere and Goodno, 2012):

$$\sigma = \frac{MC}{I} \tag{1}$$

**Table 1**
*Form 2* printer settings.

| Form 2 | Laser spot size | Laser power | Laser thickness | Operating temperature | Laser wavelength | Initial material |
|---|---|---|---|---|---|---|
| Setting | 140 μm | 250 mW | 25–300 μm | 35 °C | 405 nm | Rigid Resin |

**Table 2**
Designation, weight and density of different specimens.

| Samples | | Outside cylinders exist | Thickness of cylinders (mm) | Number of cylinders | Core | Core diameter (mm) | Weight (g) | Density (g/cm$^3$) |
|---|---|---|---|---|---|---|---|---|
| Group 1 | **SP1-3** | ✓ | 0.35 | 1 | ✓ | 9.3 | 17.38 ± 0.20 | 1.30 ± 0.03 |
| | **SP2-3** | ✓ | 0.35 | 2 | ✓ | 8.6 | 17.2 ± 0.17 | 1.28 ± 0.01 |
| | **SP3-3** | ✓ | 0.35 | 3 | ✓ | 7.9 | 16.73 ± 0.12 | 1.25 ± 0.02 |
| | **SP4-3** | ✓ | 0.35 | 4 | ✓ | 7.2 | 16.55 ± 0.10 | 1.24 ± 0.01 |
| | **SP5-3** | ✓ | 0.35 | 5 | ✓ | 6.5 | 16.39 ± 0.13 | 1.22 ± 0.01 |
| | **SP6-3** | ✓ | 0.35 | 6 | ✓ | 5.8 | 16.19 ± 0.12 | 1.21 ± 0.01 |
| | **SP7-3** | ✓ | 0.35 | 7 | ✓ | 5.1 | 16.07 ± 0.14 | 1.20 ± 0.03 |
| | **SP8-3** | ✓ | 0.35 | 8 | ✓ | 4.4 | 15.9 ± 0.09 | 1.19 ± 0.02 |
| | **SP9-3** | ✓ | 0.35 | 9 | ✓ | 3.7 | 15.76 ± 0.08 | 1.18 ± 0.01 |
| | **C1-3** | × | × | × | ✓ | 9.3 | 16.04 ± 0.10 | 1.39 ± 0.01 |
| | **C2-3** | × | × | × | ✓ | 8.6 | 13.71 ± 0.12 | 1.39 ± 0.02 |
| | **C3-3** | × | × | × | ✓ | 7.9 | 11.54 ± 0.11 | 1.35 ± 0.02 |
| | **C4-3** | × | × | × | ✓ | 7.2 | 9.61 ± 0.12 | 1.38 ± 0.01 |
| | **C5-3** | × | × | × | ✓ | 6.5 | 7.83 ± 0.12 | 1.37 ± 0.01 |
| | **C6-3** | × | × | × | ✓ | 5.8 | 6.24 ± 0.10 | 1.37 ± 0.01 |
| | **C7-3** | × | × | × | ✓ | 5.1 | 4.82 ± 0.10 | 1.38 ± 0.01 |
| | **C8-3** | × | × | × | ✓ | 4.4 | 3.59 ± 0.10 | 1.39 ± 0.01 |
| | **C9-3** | × | × | × | ✓ | 3.7 | 2.53 ± 0.06 | 1.38 ± 0.01 |
| | **CY1-3** | ✓ | 0.35 | 1 | × | × | 1.51 ± 0.05 | 0.66 ± 0.01 |
| Group 2 | **SP1-5** | ✓ | 0.5 | 1 | ✓ | 9 | 17.33 ± 0.07 | 1.29 ± 0.01 |
| | **SP2-5** | ✓ | 0.5 | 2 | ✓ | 8 | 16.98 ± 0.12 | 1.27 ± 0.01 |
| | **SP3-5** | ✓ | 0.5 | 3 | ✓ | 7 | 16.71 ± 0.10 | 1.25 ± 0.01 |
| | **SP4-5** | ✓ | 0.5 | 4 | ✓ | 6 | 16.21 ± 0.12 | 1.21 ± 0.01 |
| | **SP5-5** | ✓ | 0.5 | 5 | ✓ | 5 | 15.93 ± 0.11 | 1.19 ± 0.01 |
| | **SP6-5** | ✓ | 0.5 | 6 | ✓ | 4 | 15.75 ± 0.11 | 1.18 ± 0.01 |
| | **SP7-5** | ✓ | 0.5 | 7 | ✓ | 3 | 15.59 ± 0.10 | 1.16 ± 0.01 |
| | **C1-5** | ✓ | × | × | ✓ | 9 | 15.02 ± 0.13 | 1.39 ± 0.01 |
| | **C2-5** | ✓ | × | × | ✓ | 8 | 11.87 ± 0.10 | 1.38 ± 0.01 |
| | **C3-5** | ✓ | × | × | ✓ | 7 | 9.08 ± 0.10 | 1.4 ± 0.02 |
| | **C4-5** | ✓ | × | × | ✓ | 6 | 6.67 ± 0.09 | 1.39 ± 0.01 |
| | **C5-5** | ✓ | × | × | ✓ | 5 | 4.63 ± 0.10 | 1.39 ± 0.03 |
| | **C6-5** | ✓ | × | × | ✓ | 4 | 2.96 ± 0.10 | 1.38 ± 0.01 |
| | **C7-5** | ✓ | × | × | ✓ | 3 | 1.66 ± 0.10 | 1.39 ± 0.01 |
| | **CY1-5** | ✓ | 0.5 | 1 | × | × | 2.2 ± 0.06 | 0.71 ± 0.03 |
| Group 3 | **SP1-6** | ✓ | 0.65 | 1 | ✓ | 8.7 | 17.3 ± 0.16 | 1.29 ± 0.01 |
| | **SP2-6** | ✓ | 0.65 | 2 | ✓ | 7.4 | 16.72 ± 0.21 | 1.25 ± 0.01 |
| | **SP3-6** | ✓ | 0.65 | 3 | ✓ | 6.1 | 16.6 ± 0.13 | 1.24 ± 0.01 |
| | **SP4-6** | ✓ | 0.65 | 4 | ✓ | 4.8 | 16.29 ± 0.11 | 1.22 ± 0.01 |
| | **SP5-6** | ✓ | 0.65 | 5 | ✓ | 3.5 | 16.24 ± 0.11 | 1.21 ± 0.01 |
| | **C1-6** | × | × | × | ✓ | 8.7 | 14.04 ± 0.20 | 1.38 ± 0.02 |
| | **C2-6** | × | × | × | ✓ | 7.4 | 10.15 ± 0.10 | 1.36 ± 0.01 |
| | **C3-6** | × | × | × | ✓ | 6.1 | 6.90 ± 0.11 | 1.39 ± 0.01 |
| | **C4-6** | × | × | × | ✓ | 4.8 | 4.27 ± 0.15 | 1.41 ± 0.03 |
| | **C5-6** | × | × | × | ✓ | 3.5 | 2.27 ± 0.10 | 1.39 ± 0.02 |
| | **CY1-6** | ✓ | 0.65 | 1 | × | × | 2.94 ± 0.20 | 0.83 ± 0.01 |
| Solid sample | **CS** | × | × | × | × | × | 18 ± 0.21 | 1.39 ± 0.01 |

Where M is the bending moment, C is distance from the neutral axis (mm) and I is the moment of inertia (for cylinders, $I_{cy} = \frac{\pi}{64(d_2^4 - d_1^4)}$, and for core, $I_c = \frac{\pi}{64d^4}$). The strain can be calculated as follow:

$$\varepsilon = \frac{6Dd}{L^2} \tag{2}$$

Where D is the maximum deflection of the center of the beam (mm) and d is depth or thickness of the sample (mm). The elastic modulus can be calculated as:

$$E = \frac{L^3 m}{12\pi R^4} \tag{3}$$

Where m is the gradient (slope) of the initial straight-line portion of the load displacement curve (Subhash and Ridgeway, 2022). Furthermore, the absorbed energy was calculated from the area under the force-displacement curves.

### 2.4. Post processing analyses

In this study, we use the Weibull distribution as it is commonly used to model the failure times of mechanical components. The two-parameter Weibull distribution to analyze the flexural strength of CCSs and solid samples based is given by:

$$P_f = 1 - exp\left[ - \left( \sigma / \sigma_0 \right)^m \right] \tag{4}$$

Where $P_f$ is the failure probability, m is the Weibull modulus, σ is the obtained strength and $\sigma_0$ is characteristic strength (Lin et al., 2006).

Using our experimental data, we first fit a Weibull distribution to our

data and find the parameters. We then assess the goodness of fit between our dataset and the Weibull distribution by creating a Q-Q plot which compares the quantiles of our data against the quantiles expected from a Weibull distribution with the estimated parameters. Each set of our data points closely follow a straight line on the Q-Q plot, that means, the good fit is indicated for each dataset. We then plot the empirical cumulative distribution function (CDF) and compare it with the known Weibull CDF including the 95% lower and upper confidence bounds. Since one of the limitation of our study is the small sample sizes according to the cost of the experiment (n = 5 for each combination of process parameters), the confidence bounds are also checked to reflect how likely our datasets represent the true parameters. It is worth mentioning that when the shape parameter is large, a Weibull distribution turns into a normal distribution, and one may also check the two-way ANOVA to measure the differences between the means.

All data were expressed as mean ± standard deviation (SD) in each experiment. The two-way ANOVA and Tukey's HSD test were applied to analyze the measurements obtained from flexural peak load and displacement of solid rods and spicules inspired structure sample with different thicknesses. Each sample was repeated five times in our study. Differences were measured statistically significant at $P<0.05$. The error bars are used in Figures to indicate the variability or uncertainty associated with a data point or a group of data points. They have been used to display the accuracy or precision of measurements (Sadeghzade et al., 2020b).

## 3. Results and discussion

### 3.1. Flexural behavior of concentric cylindrical structures (CCSs) with core

The variation of maximum fracture load and displacement of CCSs with the number of layers are given in Fig. 2. Furthermore, the amount of maximum load and its displacement for CCSs and solid rods with different diameters from each group (Table 2 for complete information about the samples) were demonstrated in Table 3.

Notably, the solid sample experienced catastrophic failure at an displacement of 8.3 mm. In contrast, the reported displacement for CCSs was limited only to the fracture of the outermost cylinder, with subsequent internal layers sustaining the applied load and displacement until complete failure (see Table 4). Fig. 2c and e shows typical load-displacement curves of the flexural test of a solid rod vs. SP4-5 sample, respectively. As can be seen, the solid sample showed similar behavior to brittle materials. It failed catastrophically (Fig. 2c). There is not any plastic deformation and the yield and fracture load are located at the same point (point A in Fig. 2c). In the solid sample (solid sample), cracks started and developed in several locations and finally led to a complete failure of the sample (Fig. 2d). While CCS (SP4-5) failed gradually and revealed a load-displacement curve with a saw tooth shape (Fig. 2e) due to the response of the spicule structure (nested cylindrical structure) to the applied load. This indicates that the structure can absorb energy through successive layers, contributing to its resilience (Kamat et al., 2000). In this type of sample (CCSs), cracks were initiated from the tension surface of the first layer and developed in both perpendicular and parallel directions to the applied force (Fig. 2g). This behavior is attributed to the nested cylindrical structure of the spicules, where cracks are initiated and arrested between layers, allowing for load

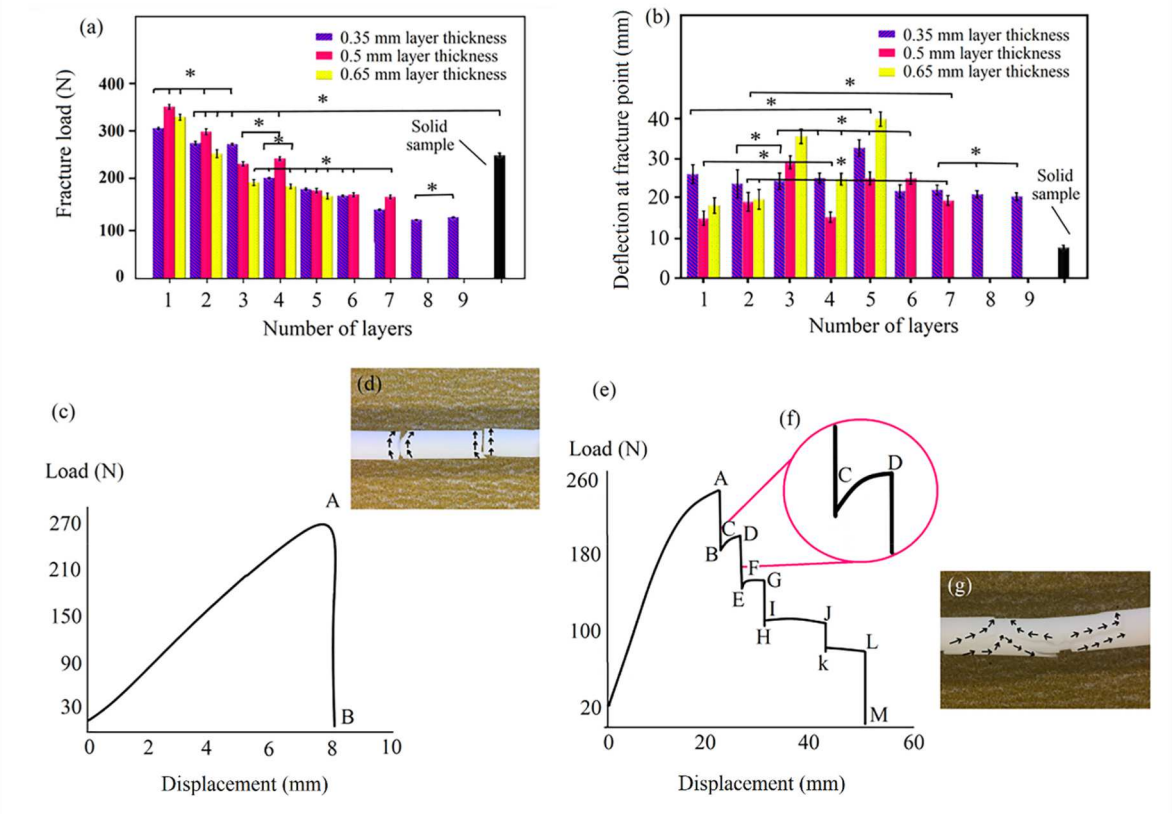


**Fig. 2.** (a) Maximum fracture load, (b) Deflection at fracture point of spicule-inspired structures (CCSs) as a function of number of layers with various thicknesses compared to solid rods (as the solid sample, *statistically not different from each other $P > 0.05$), (c) Typical load-displacement curve of a solid rod, (d) Fracture image of solid sample after bending test, (e–f) Typical load-displacement curve of SP4-5 sample, (g) Fracture image of SP4-5 sample after bending test.

**Table 3**
Load and displacement of the solid, CCSs, single cylinder and single core at fracture and ultimate points.

| Samples | Load at yield point (N) | Load at fracture point (N) | Displacement at Fracture point (mm) | Sample failed | Samples | Load at yield point (N) | Load at fracture point (N) | Displacement at Fracture point (mm) | Break of rod |
|---|---|---|---|---|---|---|---|---|---|
| SP1-3 | 272.1 ± 17.1 | 312.6 ± 11.2 | 26.2 ± 1.4 | ✓ | **SP4-5** | 189.5 ± 14.1 | 250.1 ± 12.2 | 15.6 ± 1.5 | ✓ |
| SP2-3 | 241.2 ± 14.2 | 282 ± 12 | 23.8 ± 1.6 | ✓ | **SP5-5** | 139.2 ± 10.9 | 183.5 ± 11.4 | 25.1 ± 1.6 | ✓ |
| SP3-3 | 210.1 ± 10.8 | 279.8 ± 20.9 | 24.5 ± 1.5 | ✓ | **SP6-5** | 141.2 ± 10.9 | 175 ± 12.3 | 25.1 ± 1.7 | × |
| SP4-3 | 173.6 ± 11.5 | 209.9 ± 20.9 | 25.1 ± 1.5 | ✓ | **SP7-5** | 139.2 ± 14.9 | 170.2 ± 11.2 | 19.7 ± 1.8 | × |
| SP5-3 | 171.1 ± 15.9 | 186.3 ± 14.1 | 32.5 ± 1.7 | ✓ | **C1-5** | 224.1 ± 12.1 | 231.2 ± 20.9 | 12.2 ± 0.4 | ✓ |
| SP6-3 | 145.5 ± 10.1 | 172.3 ± 16.2 | 22 ± 1.6 | ✓ | **C2-5** | 142.6 ± 10.8 | 157.2 ± 11.1 | 18.2 ± 1.3 | ✓ |
| SP7-3 | 118.6 ± 11.1 | 143.9 ± 13.1 | 22.3 ± 1.6 | ✓ | **C3-5** | 93.4 ± 11.8 | 114.6 ± 11.2 | 12.6 ± 1.2 | ✓ |
| SP8-3 | 98.8 ± 12.2 | 122.9 ± 14.2 | 21.1 ± 1.4 | ✓ | **C4-5** | 34.4 ± 4.1 | 56.1 ± 5.8 | 9.9 ± 1.0 | ✓ |
| SP9-3 | 95.5 ± 10.9 | 127.9 ± 15.2 | 20.6 ± 1.5 | ✓ | **C5-5** | 23.2 ± 3.9 | 35 ± 3.3 | 12.2 ± 1.1 | ✓ |
| C1-3 | 236.8 ± 20.9 | 245.2 ± 12.1 | 11.6 ± 1.2 | ✓ | **C6-5** | 16 ± 1.2 | – | – | × |
| C2-3 | 192.3 ± 11.1 | 201.1 ± 10.9 | 13.4 ± 1.3 | ✓ | **C7-5** | 7.1 ± 2.1 | – | – | × |
| C3-3 | 154.1 ± 10.9 | 182 ± 12.2 | 13.1 ± 1.1 | ✓ | **CY1-5** | 12.2 ± 2.2 | – | – | × |
| C4-3 | 121.3 ± 21 | 138.9 ± 10.9 | 10.9 ± 1.3 | ✓ | **SP1-6** | 269.4 ± 16.1 | 335.9 ± 20.7 | 18.5 ± 1.7 | ✓ |
| C5-3 | 72.3 ± 6.5 | 96.6 ± 11.1 | 13.1 ± 1.2 | ✓ | **SP2-6** | 212.9 ± 17.5 | 260 ± 21.1 | 20 ± 1.2 | ✓ |
| C6-3 | 28.2 ± 3.4 | 32.3 ± 5.2 | 13.5 ± 1.2 | ✓ | **SP3-6** | 165.4 ± 13.1 | 200.8 ± 21.4 | 35.4 ± 1.6 | ✓ |
| C7-3 | 25.3 ± 5.5 | 17.5 ± 3.2 | 28.2 ± 2.1 | × | **SP4-6** | 159.5 ± 15.4 | 192.5 ± 21.3 | 24.9 ± 1.4 | × |
| C8-3 | 21 ± 2.1 | – | – | × | **SP5-6** | 155.2 ± 13.2 | 171.9 ± 21.2 | 39.5 ± 2.5 | × |
| C9-3 | 9.3 ± 1.5 | – | – | × | | | | | ✓ |
| CY1-3 | 8.5 ± 1.4 | – | – | × | **C2-6** | 200.2 ± 21.1 | 226.2 ± 17.2 | 12.5 ± 1.3 | ✓ |
| SP1-5 | 249.2 ± 21.3 | 357.3 ± 17.1 | 15.4 ± 0.6 | ✓ | **C3-6** | 134.5 ± 21 | 152.9 ± 15.6 | 13.3 ± 1.1 | ✓ |
| SP2-5 | 251.6 ± 23.4 | 305.8 ± 15.2 | 19.4 ± 0.8 | ✓ | **C4-6** | 68.3 ± 5.1 | 81.3 ± 9.3 | 12.2 ± 1.3 | ✓ |
| SP3-5 | 195.5 ± 17.1 | 238.8 ± 17.5 | 29.1 ± 2.5 | ✓ | **C5-6** | 6.6 ± 1.3 | – | – | × |
| C1-6 | 201.3 ± 21.3 | 231.2 ± 14.9 | 12.2 ± 1.4 | ✓ | **CY1-6** | 21.4 ± 2.4 | – | – | × |
| | | | | ✓ | **CS** | 269.3 ± 14.4 | 269.3 ± 14.4 | 8.1 ± 1.2 | 8.1 ± 1.21 |

**Table 4**
Failure of the core and concentric cylindrical layers in various samples.

| Samples | Number of layers | Solid core diameter (mm) | Shattered layer | Shattered core |
|---|---|---|---|---|
| SP1-3 | 1 | 9.3 | ✓ | ✓ |
| SP2-3 | 2 | 8.6 | ✓ | ✓ |
| SP3-3 | 3 | 7.2 | ✓ | ✓ |
| SP4-3 | 4 | 6.5 | ✓ | ✓ |
| SP5-3 | 5 | 5.8 | ✓ | × |
| SP1-5 | 1 | 9 | ✓ | ✓ |
| SP2-5 | 2 | 8 | ✓ | ✓ |
| SP3-5 | 3 | 7 | ✓ | ✓ |
| SP4-5 | 4 | 6 | ✓ | ✓ |
| SP5-5 | 5 | 5 | ✓ | × |
| SP1-6 | 1 | 8.7 | ✓ | ✓ |
| SP2-6 | 2 | 7.4 | ✓ | ✓ |
| SP3-6 | 3 | 6.1 | ✓ | ✓ |
| SP4-6 | 4 | 4.8 | ✓ | × |
| SP5-6 | 5 | 3.5 | ✓ | × |

redistribution and delaying catastrophic failure (Chai and Ravichandran, 2007; Lugovy et al., 2005)

As a result, a sudden drop in the curve occurred (section AB in Fig. 2e). In the next step, the second layer initially underwent an elastic deformation (section BC in Fig. 2e) under the influence of applied force and then showed the plastic deformation (section CD in Fig. 2e) and finally failed (section DE). The graph's C, F, and I points show the yield point in each layer. The same procedure happened for the rest of the layers until the core was broken (section LM). These results agree with the mechanical behavior of natural spicules. As can be seen, CCSs demonstrated more flexibility compared to the solid samples.

Also, CCSs increased the total displacement at the final fracture point (from 8 mm for the solid rod to about 50 mm for SP4-5). The deflection at the final fracture point reached for the samples with higher number of layers 60 mm. The maximum load and deflection at yield and fracture point of solid rods with various diameters (C1-3 to C9-3 samples) are presented in Table 3. These samples have the same diameter as the core of CCSs in each group. The combination of a core with concentric cylinders, similar to natural spicule structures, results in an excellent combination of strength, toughness, and flexibility. While the core and cylinders, separately (see Table 3), cannot show the same mechanical properties. This underscores the importance of the structure of spicules in optimizing mechanical properties for specific functional requirements.

### 3.2. *Mechanical properties of concentric cylindrical structures (CCSs) with core*

The influence of thickness and number of layers on the flexural behavior of concentric cylindrical structures (CCSs) compared to solid samples is depicted in Fig. 3a–d. CCSs with 1–4 layers show specific strength comparable or superior to solid samples, with significantly higher strains, crucial for fabricating lightweight structures with superior mechanical properties. It should be mentioned that the specific properties of materials, particularly the specific strength, are an important factor in fabricating lightweight structures with high mechanical properties such as high strength, strain, modulus, and absorbed energy (Yancey, 2016). The concentric cylindrical structure distributes stress effectively, reducing crack propagation and enhancing absorbed energy and strain properties compared to solid sample.

SP5-3 (6.39 ± 0.73 %), SP3-5 (5.62 ± 0.61%) and SP3-6 (6.88 ± 0.93%) samples with 5, 3 and 3 layers, respectively, showed 228%, 188%, and 253% improvement in the strain at fracture point only for the failure of the outer layer compared to the solid samples (1.95 ± 0.23%). Also, as shown in Fig. 3c, in all CCSs with a different number of layers and thicknesses, the absorbed energy was more than the solid sample (1.01 ± 0.32 KJ). Specifically, an increase of 484% and 473% in absorbed energy for both SP4-3 (5.9 ± 0.4 KJ) and SP3-6 (5.7 ± 0.7 KJ) samples was achieved compared to the solid sample.

The enhanced absorbed energy observed in the CCSs can be attributed to several mechanisms inherent in their concentric cylindrical structure. Firstly, the presence of concentric layers introduces multiple interfaces and discontinuities, which act as barriers to crack propagation. As cracks encounter these interfaces, they are deflected, redirected, or trapped within the layers, thereby dissipating energy and preventing catastrophic failure. Additionally, the frictional forces between adjacent layers and core serve to impede crack propagation by resisting crack advancement. Moreover, the bridging effect between layers, where cracks are bridged or bridging elements form across cracked regions,

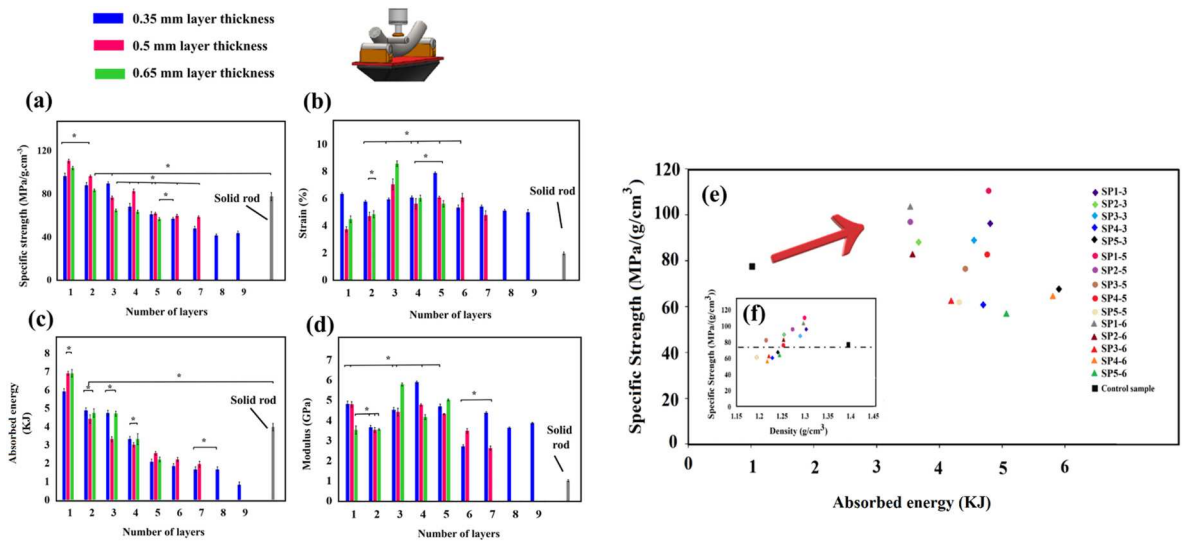


**Fig. 3.** Comparison of (a) Specific strength, (b) Strain, (c) Absorbed energy, (d) Modulus of CCSs as a function of number of layers and various thicknesses vs solid rods (*statistically not different from each other $P > 0.05$), (e) Comparison of specific strength as a function of absorbed energy of CCSs up to 5 layers as well as solid rods and, (f) Specific strength of CCSs as well as solid rods as a function of density.

further contributes to crack arrest and energy dissipation. Lastly, the trapping mechanism involves the entrapment of crack tips within the layered structure, effectively halting their progression and promoting ductile behavior. Collectively, these mechanisms synergistically enhance the absorbed energy of the spicule-inspired structures, making them resilient to mechanical stress and deformation (Sadeghzade et al., 2020a). The absorbed energy improvements, as high as 484% and 473% in samples like SP4-3 and SP3-6, underscore the significant advantages of CCSs for optimizing mechanical properties.

Fluctuations in the curve result from systematic variations in parameters like the number of layers, core size, and thickness, altering mechanical behavior along the curve. The core in CCSs serves as central support, affecting stress distribution and response to loads. Varying core sizes can impact stiffness and flexibility; larger cores make CCSs stiffer with lower absorbed energy and strain, while smaller cores increase flexibility. Core presence influences crack initiation and propagation within CCSs. A smaller core might provide more reinforcement and deter cracks from propagating rapidly, leading to higher absorbed energy and strain (Sadeghzade et al., 2017).

A larger core may lead to faster crack propagation, altering mechanical behavior. Decreasing modulus trends were observed in CCSs with more than 4 layers, indicating increased flexibility. Specific strength and absorbed energy showed optimal combinations in CCSs with 1–3, 1–4, and 1–2 layers, respectively. Among CCSs, SP4-5 maintained high specific strength (82.57 ± 15.21 MPa) compared to solid samples, while SP4-3 and SP4-6 exhibited 13% and 19% lower specific strength. CCSs demonstrated lower density than solid samples, with the lowest density in samples with the highest number of layers. Transitioning from solid rods to CCSs shifted fracture mode from catastrophic failure to gradual failure with energy absorption capability.

In a study the micromechanical properties of silica spicules from EA were characterized in dry and water environments using nano-indentation experiments. The results showed that the concentric layers surrounding the central core were softer and more compliant, while the central core provided rigidity to the spicule. The properties of the central core remained unchanged in the presence of water, indicating that it was already hydrated. However, the layered regions exhibited a decrease in Young's modulus and hardness due to the plasticization of the organic interlayers. Further exposure to water did not cause additional changes in the spicule's properties (Morankar et al., 2023). Several studies have investigated the micromechanical and fracture behavior of natural EA spicule structure (Mayer and Zhou, 2009; Miserez et al., 2008; Monn and Kesari, 2017; Morankar et al., 2022).

### 3.3. Crack propagation model of concentric cylindrical structures (CCSs) with core

The model of crack propagation and failure mechanism of CCSs with a different number of layers as well as the solid samples (solid rods) were presented in Fig. 4a. As seen, when the solid sample is subjected to bending test, cracks nucleate on the outer surface which is under tension. With increasing the bending force, the shear stresses created on the cross section of the sample increase and result in crack propagation. Since there is no obstacle to stop the crack propagation, cracks grow rapidly, and the material collapses abruptly in several areas (Hashemian et al., 2022). While, In CCSs, the presence of a layered structure is the main factor to prevent catastrophic failure. This type of structure can absorb energy and change the mode of fracture from catastrophic to gradual failure by deflecting the crack from one layer to the successive layer (Fig. 4a and b). After failure of the first layer, initiation of a new crack in the successive layer needs more energy which consequently increases the strength of the entire structure. The crack nucleation occurs on the first layer which is under tension. The cracks propagate along the thickness of the first layer (parallel to the direction of the load) and are deflected and/or stopped at the interface of first and second cylinders (Fig. 4a). Consequently, more load is required to initiate new cracks in the following cylinders resulting an increased toughness in CCSs compared to solid rods. As shown in Fig. 4a, with increasing the number of layers around the core, the number of interfaces increased and the movement of crack throughout the sample became more difficult.

Subsequently, cracks were arrested and faced more interfaces and the toughness increased. The shear stress distribution of CCSs compared to solid samples (solid rods) is illustrated in Fig. 4c. If we consider the rod's circular cross section during the bending test, a positive shear load (V) is created on the cross section of the rod. As a results of shear load, the transverse shear stress act on the cross section which is parallel to the shear load direction (Gere and Goodno, 2012). If we consider a small element of the sample, the transverse shear stresses should act on the front and back surfaces of this element (Fig. 4a). Other shear stresses with the same magnitude of transverse shear stress act on the top and bottom surface of the element which is called the longitudinal shear stress (Fig. 4a) (Gere and Goodno, 2012). Therefore, longitudinal shear stresses act between the layer's trough the length of cylinders and the transvers shear stresses act along the cross section (along the thickness)

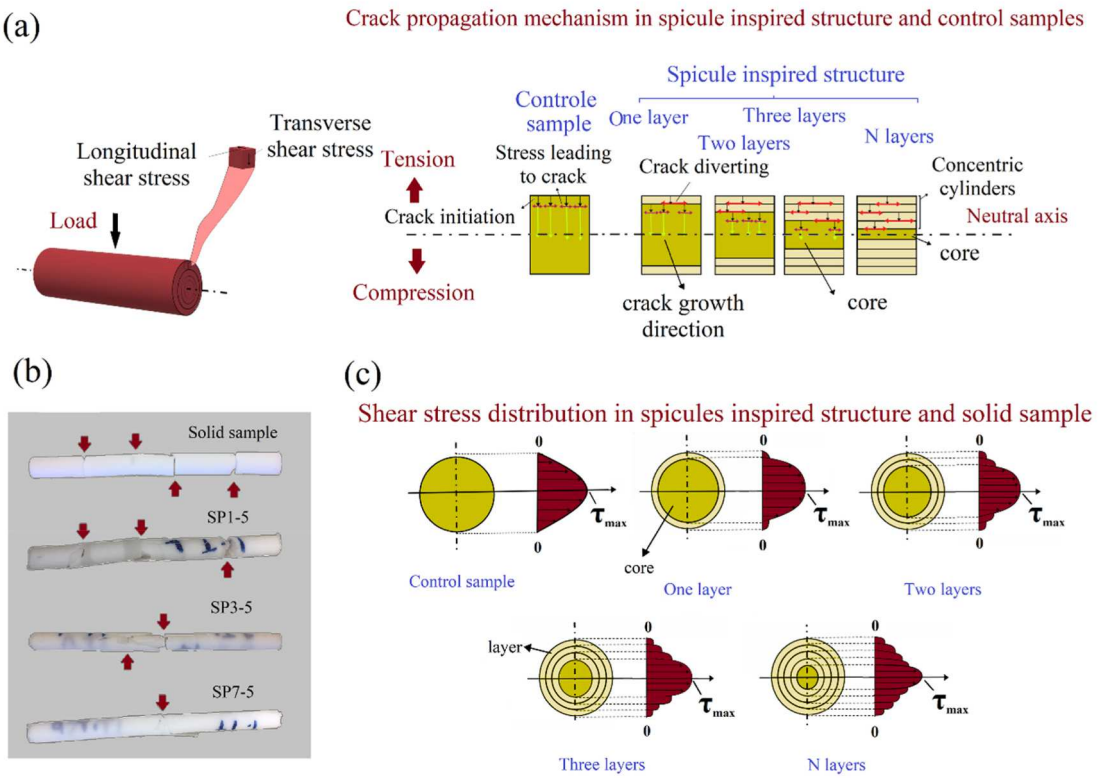


**Fig. 4.** (a) Crack propagation through the solid rod vs spicule-inspired structures with different number of layers under bending test, (b) Images of the fractured specimens with cylindrical layer thickness of 0.5 mm containing 1, 3 and 7 cylindrical layers compared to solid rods, (c) Typical shear stress distribution in a solid rod vs spicule-inspired structures with different number of layers under bending test.

of each cylinder (Gere and Goodno, 2012). The distribution of shear stresses can be explained by the shear formula (Gere and Goodno, 2012) which determine the shear stresses at each point in the cross section (Fig. 4). By looking at the solid samples, the shear stress on the top and bottom surfaces are zero, while, the maximum amount of shear stress is observed on the neutral axis (Oskui et al., 2022). While, in CCSs, at the interfaces of cylinders, the shear stresses cannot reach the zero-value due to the presence of friction in between layers under applying pressure.

Controlling the number and size of cracks and their propagation in the microstructure plays a vital role in the toughness of brittle materials. According to Griffith's equation (Gere and Goodno, 2012):

$$\sigma_y = \left(\frac{2\gamma E}{\pi c}\right)^{\frac{1}{2}} \tag{5}$$

where $\sigma_y$ is the fracture stress, γ is surface energy, E is the elastic modulus and c is the existing crack length, when a crack is created in an integrated structure, to grow and break the structure, the size of the crack has to go beyond a critical value. On the other hand, larger cracks require less energy to grow and develop throughout the structure (Es'haghi Oskui et al., 2019). While, in materials with spicule inspired structure, when a crack is nucleated on the surface of the outer layer, no matter how large it is, it will stop at the interface of the next layer, and therefore new cracks should be initiated on the new layer which requires more energy (Oskui et al., 2014).

With increasing the number of layers in CCSs with 1, 3 and 7 layers (with layer thickness of 0.5 mm) the absorbed energy and toughness increased. As a result, with reducing the core size (Table 3), fracture just happened in some outer layers (for example in SP7-5). However, in samples with 1 and 3 layers with a larger core, the samples were shattered from several locations. Increasing the number of layers to 7 had a higher impact on the flexural strength of the CCSs. In SP3-5 sample, the failure was started from the core. While in samples with 7 layers (SP7-5) the crack always started from the outer layer. Similar mechanism was reported for strengthening and toughening of natural rigid composite materials such as nacre (mollusk) and sponge spicules (Gere and Goodno, 2012). Researchers have reported that the energy dissipation in natural rigid biological structures can happen through creation of new surfaces (for example by designing layered structures), delamination of the organic layers (organic layer bridging), crack deflection, and crack bridging (Gere and Goodno, 2012; Mayer, 2011; Zhao et al., 2018). By comparing the results of mechanical properties of spicule-inspired structure with natural ones, it can be understood that the presence of a thin organic layer between the cylinders is not the only reason for the excellent mechanical properties of spicules. In fact, the results of mechanical properties of CCSs confirmed that the microstructure of CCSs and the presence of a nested concentric cylindrical structures can be as important as the presence of organic layers and can play a vital role in the mechanical properties of CCSs (Lugovy et al., 2005).

### *3.4. Impact of layer count and core presence on flexural behavior of concentric cylindrical structures (CCSs)*

The load-displacement curves of CCSs with varying thicknesses and numbers of layers are presented in Fig. 5a–c. Increasing layer thickness shifted the fracture mechanism from catastrophic to gradual, as observed in SP1-3, SP1-5, and SP1-6. Additionally, samples with 0.35 mm and 0.5 mm layer thickness demonstrated a more gradual fracture compared to those with 0.65 mm thickness, regardless of the number of layers.

The SP5-6 sample unexpectedly fractured abruptly at point A, indicating a deviation from the anticipated gradual fracture pattern. This sudden failure suggests a shift in the energy dissipation model due to

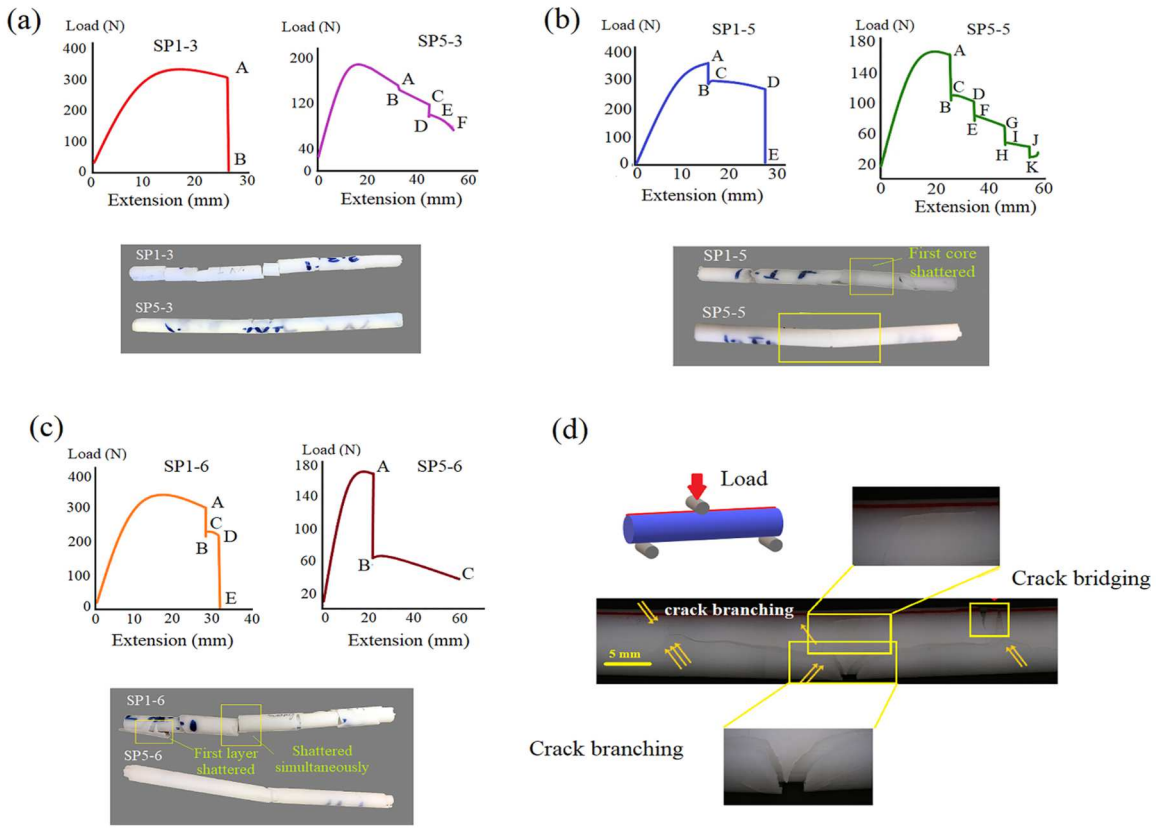


**Fig. 5.** Typical load-displacement curve of CCSs as well as fractured samples with (a) 0.35 mm, (b) 0.5 mm, (c) 0.65 mm wall thicknesses under bending test, (d) Optical microscopic images of SP5-5 after bending test.

changes in layer thickness and count. Additionally, fracture and deformation mechanisms involve various energy dissipation pathways, including crack deflection, bridging, delamination, and viscoelastic deformation, highlighting the complex interplay of factors influencing the structural integrity of the specimen. (Chen et al., 2012; Monn et al., 2020).

During the bending test, samples with higher thickness and number of layers exhibited sliding and delamination across multiple layers simultaneously. Increasing layer thickness diminished crack deflection effectiveness, leading to simultaneous failure of several cylinders. Conversely, samples with smaller cylinder wall thickness experienced individual layer breakage. Fracture patterns varied among single-layered samples, with the solid core or outer cylinder breaking first or both simultaneously. This phenomenon was observed in samples with 4, 4, and 3 layers, respectively, corresponding to core sizes exceeding 6 mm, which caused the sample behavior to resemble that of solid rods.

By reducing the size of the solid core to less than 6 mm, flexibility increased while the likelihood of solid core failure decreased. Consequently, in samples with a higher number of layers and a smaller solid core diameter, sliding and delamination mechanisms were activated. Various toughening and strengthening mechanisms were observed in spicule-inspired structures, including crack branching, deflection, and bridging. Crack branching indicates a significant role in materials failure, facilitating energy release and stress reduction. Unlike single-layered samples where cracks propagated directly, CCSs with more layers exhibited a changed fracture mechanism. In these samples, cracks initiated along the diameter but failed by either creating new cracks in the next layer or by branching along the length of the sample in the first layer, resulting in enhanced absorbed energy (Lin et al., 2006; Yang et al., 2019). As can be seen in Fig. 5a–c (images of the samples after bending test), for the samples with only one layer around the solid core, crack branching did not occur and cracks were developed directly along the cross section of the specimens (similar to the solid sample, Fig. 2d). Whereas, in CCSs with more layers (5 layers) the fracture mechanism was changed. In those samples, cracks initially started along the diameter of CCSs and led to fracture of the first layer; however, because of the discontinuity of the structure (the presence of a layered structure) the samples failed either by applying more energy to create new cracks in the next layer or by crack branching along the length of the sample in the first layer (which required less energy to propagate the crack). As can be seen in Fig. 5d, the crack in SP5-5 sample was branched along the longitudinal direction rather than propagating into the second layer which resulted in a higher absorbed energy in the structure.

### 3.5. *Analysis of flexural strength distribution of concentric cylindrical structures (CCSs)*

The Weibull analysis diagrams (failure probability as a function of flexural strength) are shown in Fig. 6a–c for CCSs with 0.35, 0.5 and 0.65 mm wall thickness containing up to 5 cylindrical layers compared to the solid rod (CS). Also, the flexural strength of different samples at 50% failure probability is presented in Table 5.

For the CCSs with 0.35 mm wall thickness, the 50% failure probability [$P_f = 0.5$] for the flexural strength for SP1-3, SP2-3 and SP3-3 samples were 122.6, 108.3 and 99.6 MPa, respectively. Compared to CS, the improvement of flexural strength at 50% $P_f$ for SP1-3, SP2-3 and SP3-3 were approximately 31, 15, 6%. With increasing the wall thickness to 0.5 and 0.65 mm the flexural strength of SP1-5, SP2-5, SP1-6 and SP2-6 were showed 50% failure probability at 137.8, 114.2, 129.9 and 99.3 MPa, respectively. It seems that changing the solid structure to the spicule-inspired structure reduces the 50% failure probability. CCSs showed an improvement up to 47% for 50% failure probability of

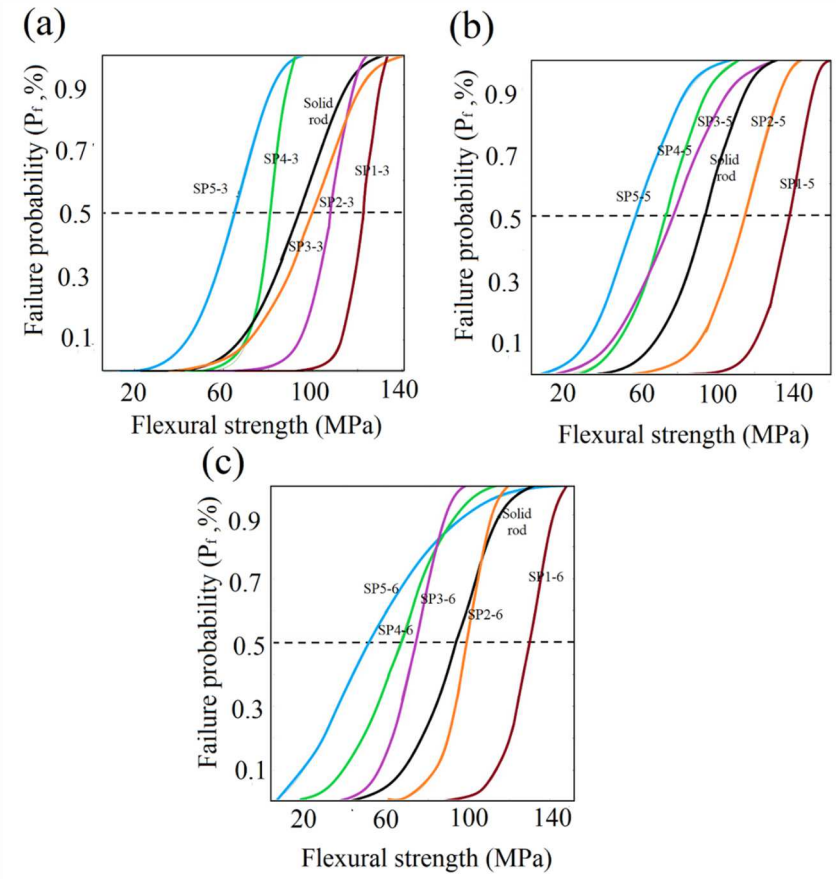


**Fig. 6.** Weibull plot of CCSs (a) Group 1, (b) Group 2 and, (c) Group 3 up to 5 layers compared to solid rods.

**Table 5**
The flexural strengths at 50% failure probability for different samples.

| Samples | Flexural strength at 50% $P_f$ (MPa) |
|---|---|
| SP1-3 | 122.6 |
| SP2-3 | 108.3 |
| SP3-3 | 99.6 |
| SP4-3 | 81.08 |
| SP5-3 | 64.34 |
| SP1-5 | 137.8 |
| SP2-5 | 114.2 |
| SP3-5 | 77.43 |
| SP4-5 | 74.07 |
| SP5-5 | 58.92 |
| SP1-6 | 129.9 |
| SP2-6 | 99.32 |
| SP3-6 | 74.07 |
| SP4-6 | 65.93 |
| SP5-6 | 51.34 |
| CS | 93.99 |

flexural strength. By considering the flexural strength of the solid rod at 50% failure probability, it can be seen that increasing the wall thickness to 0.5 and 0.65 mm led to a sudden decrease in the flexural strength at 50% $P_f$. While, in the sample with 0.35 mm thickness, a gradual decrease was observed. Even the sample with 3 layer and 0.35 mm thickness was still able to show acceptable strength at 50% failure probability compared to CS. The samples with thickness of 0.35 mm could maintain the appropriate level of flexural strength at 50% $P_f$ up to more layers around the core and prevent the sudden dropping of flexural strength at 50% $P_f$.

## 4. Conclusions

Spicule-inspired structures were successfully fabricated by SLA technique with rigid resin after curing process. A higher amount of absorbed energy (4–6 times more than that of solid rods) was observed for all the spicule-inspired structures compared to the solid rods. The results showed that using a concentric cylindrical structure decreased the weight of the samples as well as their density due to formation of some gaps in between the layers. Around 10% reduction in weight was observed for CCSs with 4 and 5 cylindrical layers with a 0.5 mm layer thickness compared to the solid rods. The specific flexural strength, strain, absorbed energy and modulus of SP4-5 (the optimum sample) was 82.57 ± 15.21 MPa/g.cm$^{-3}$, 4.61 ± 0.53 1/g.cm$^{-3}$, 4.77 ± 0.61 KJ and 2.48 ± 0.1 GPa/g.cm$^{-3}$, respectively. Compared to the solid rods, SP4-5 sample showed a more flexible structure (13% reduction in modulus) with 7 %, 230 % and 372 % improvement in the specific flexural strength, strain and absorbed energy, respectively. Based on the Weibull distribution, the failure probability (in 50% fracture) of CCSs with 4, 2 and 2 layers and less from group 1, 2 and 3 was higher than the solid samples. This study shows that the spicule inspired structures create some obstacles in the crack development path of brittle materials which exhibit some extent of flexible. Also, observation of the fracture behavior of CCSs sample as compared to solid sample of brittle rigid resin shows that the CCSs can withstand higher loads and provide a safer structure even in the case of fracture.

## CRediT authorship contribution statement

**Fariborz Tavangarian:** Writing – review & editing, Writing – original draft, Validation, Supervision, Software, Resources, Project

administration, Methodology, Funding acquisition, Data curation, Conceptualization. **Sorour Sadeghzade:** Writing – review & editing, Writing – original draft, Validation, Software, Methodology, Investigation, Conceptualization. **Niloofar Fani:** Software, Formal analysis. **Dariush Khezrimotlagh:** Validation, Software, Formal analysis. **Keivan Davami:** Writing – review & editing, Software, Formal analysis.

## Declaration of competing interest

The authors declare that they have no known competing financial interests or personal relationships that could have appeared to influence the work reported in this paper.

## Data availability

Data will be made available on request.

## Acknowledgements

This project was partially supported by the NSF-CAREER under the NSF Cooperative Agreement CMMI-2146480. Also, this project was made possible, in part, by a seed grant from Penn State Harrisburg's Office of Research and Outreach.

## Appendix A. Supplementary data

Supplementary data to this article can be found online at https://doi.org/10.1016/j.jmbbm.2024.106555.

## References

Adibeig, M.R., Vakili-Tahami, F., Saeimi-Sadigh, M.-A., 2023. Numerical and experimental investigation on creep response of 3D printed Polylactic acid (PLA) samples. Part I: the effect of building direction and unidirectional raster orientation. J. Mech. Behav. Biomed. Mater. 145, 106025 https://doi.org/10.1016/j.jmbbm.2023.106025.

Barthelat, F., 2023. The fracture mechanics of biological materials. In: Ponson, L. (Ed.), Mechanics and Physics of Fracture, CISM International Centre for Mechanical Sciences. Springer International Publishing, Cham, pp. 255–282. https://doi.org/10.1007/978-3-031-18340-9_4.

Chai, H., Ravichandran, G., 2007. Transverse fracture in multilayers from tension and line-wedge indentation. Int. J. Fract. 145, 299–312. https://doi.org/10.1007/s10704-007-9129-7.

Chen, P.-Y., McKittrick, J., Meyers, M.A., 2012. Biological materials: functional adaptations and bioinspired designs. Prog. Mater. Sci. 57, 1492–1704. https://doi.org/10.1016/j.pmatsci.2012.03.001.

Das, S., 2001. The Cost of Automotive Polymer Composites: a Review and Assessment of DOE's Lightweight Materials Composites Research. Oak Ridge National Laboratory, Oak Ridge, TN, USA.

Es'haghi Oskui, A., Soltani, N., Rajabi, M., Schmauder, S., 2019. Mixed-mode fracture behavior of AM60 magnesium alloy using two parameter fracture mechanics. Eng. Fract. Mech. 218, 106566 https://doi.org/10.1016/j.engfracmech.2019.106566.

Flexural Strength of Ceramic and Glass Rods [WWW Document], n.d. URL https://www.astm.org/jte101649.html (accessed 11.September.2023).

Gere, J.M., Goodno, B.J., 2012. Mechanics of Materials. Cengage learning.

Hashemian, S., Keshtiban, P.M., Oskui, A.E. haghi, 2022. Fracture behavior of the forged aluminum 7075-T6 alloy under mixed-mode loading conditions. Eng. Fail. Anal. 140, 106610.

Hassanifard, S., Adibeig, M.R., Hashemi, S.M., 2022. Determining strain-based fatigue parameters of additively manufactured Ti–6Al–4V: effects of process parameters and loading conditions. Int. J. Adv. Manuf. Technol. 121, 8051–8063. https://doi.org/10.1007/s00170-022-09907-5.

Jin, L., Zhang, M., Shang, L., Liu, L., Li, M., Ao, Y., 2020. A nature-inspired interface design strategy of carbon fiber composites by growing brick-and-mortar structure on carbon fiber. Compos. Sci. Technol. 200, 108382.

Joshi, M., Chatterjee, U., 2016. Polymer nanocomposite: an advanced material for aerospace applications. In: Advanced Composite Materials for Aerospace Engineering. Elsevier, pp. 241–264.

Kamat, S., Su, X., Ballarini, R., Heuer, A.H., 2000. Structural basis for the fracture toughness of the shell of the conch Strombus gigas. Nature 405, 1036–1040.

Lin, A.Y.M., Meyers, M.A., Vecchio, K.S., 2006. Mechanical properties and structure of Strombus gigas, Tridacna gigas, and Haliotis rufescens sea shells: a comparative study. Mater. Sci. Eng. C 26, 1380–1389.

Lugovy, M., Slyunyayev, V., Orlovskaya, N., Blugan, G., Kuebler, J., Lewis, M., 2005. Apparent fracture toughness of Si3N4-based laminates with residual compressive or tensile stresses in surface layers. Acta Mater. 53, 289–296.

Luz, G.M., Mano, J.F., 2009. Biomimetic design of materials and biomaterials inspired by the structure of nacre. Phil. Trans. R. Soc. A. 367, 1587–1605. https://doi.org/10.1098/rsta.2009.0007.

Mayer, G., 2011. New toughening concepts for ceramic composites from rigid natural materials. J. Mech. Behav. Biomed. Mater. 4, 670–681.

Mayer, G., Trejo, R., Lara-Curzio, E., Rodriguez, M., Tran, K., Song, H., Ma, W.H., 2004. Lessons for new classes of inorganic/organic composites from the spicules and skeleton of the sea sponge. In: Euplectella Aspergillum, vol. 844. MRS Online Proceedings Library (OPL).

Mayer, G., Zhou, J., 2009. The role of the organic component in the mechanical behavior of biomineralized composites. MRS Online Proc. Libr. 1187, 1187. KK07.

Minchin, E.A., 1909. Sponge-spicules. Ergebn Fortschr Zoologie 2, 171–274.

Mirkhalaf, M., Men, Y., Wang, R., No, Y., Zreiqat, H., 2023. Personalized 3D printed bone scaffolds: a review. Acta Biomater. 156, 110–124.

Miserez, A., Weaver, J.C., Thurner, P.J., Aizenberg, J., Dauphin, Y., Fratzl, P., Morse, D. E., Zok, F.W., 2008. Effects of Laminate architecture on fracture resistance of sponge Biosilica: Lessons from nature. Adv. Funct. Mater. 18, 1241–1248. https://doi.org/10.1002/adfm.200701135.

Monn, M.A., Kesari, H., 2017. Enhanced bending failure strain in biological glass fibers due to internal lamellar architecture. Journal of the Mechanical Behavior of Biomedical Materials, Structure-Property Relationships in Biological and Bioinspired Materials 76, 69–75. https://doi.org/10.1016/j.jmbbm.2017.05.032.

Monn, M.A., Vijaykumar, K., Kochiyama, S., Kesari, H., 2020. Lamellar architectures in stiff biomaterials may not always be templates for enhancing toughness in composites. Nat. Commun. 11 https://doi.org/10.1038/s41467-019-14128-8.

Morankar, S., Kumar, A., Luktuke, A., Chawla, N., 2023. Influence of hydration on the micromechanical properties of silica spicules from the Venus flower basket (Euplectella aspergillum). JOM 75, 3816–3826. https://doi.org/10.1007/s11837-023-05966-5.

Morankar, S., Singaravelu, A.S.S., Niverty, S., Mistry, Y., Penick, C.A., Bhate, D., Chawla, N., 2022. Tensile and fracture behavior of silica fibers from the Venus flower basket (Euplectella aspergillum). Int. J. Solid Struct. SI (Jim Barber's 80thbirthday Special Issue 253), 111622 https://doi.org/10.1016/j.ijsolstr.2022.111622.

Murr, M.M., 2006. Protein Fiber Formation in Silica Biomineralization: A New Path to Hierarchical Assembly and Emergent Properties. University of California, Santa Barbara.

Oskui, A.E., Choupani, N., Haddadi, E., 2014. Experimental and numerical investigation of fracture of ABS polymeric material for different sample's thickness using a new loading device. Polym. Eng. Sci. 54, 2086–2096. https://doi.org/10.1002/pen.23745.

Oskui, A.E. haghi, Haddadi, E., Ebrahimi, M., 2022. A technical approach toward pre-crack generation and its effect on the fracture behavior of polymeric materials. Eng. Fract. Mech. 274, 108780.

Robson Brown, K., Bacheva, D., Trask, R.S., 2019. The structural efficiency of the sea sponge *Euplectella aspergillum* skeleton: bio-inspiration for 3D printed architectures. J. R. Soc. Interface. 16, 20180965 https://doi.org/10.1098/rsif.2018.0965.

Sadeghzade, S., Emadi, R., Salehi, M., Tavangarian, F., Ramini, A., 2020a. Crack propagation and toughening mechanisms of bio-inspired artificial spicules fabricated by additive manufacturing technique. Theor. Appl. Fract. Mech., 102797

Sadeghzade, S., Emadi, R., Tavangarian, F., Doostmohammadi, A., 2020b. The influence of polycaporolacton fumarate coating on mechanical properties and in vitro behavior of porous diopside-hardystonite nano-composite scaffold. J. Mech. Behav. Biomed. Mater. 101, 103445.

Sadeghzade, S., Emadi, R., Tavangarian, F., Naderi, M., 2017. Fabrication and evaluation of silica-based ceramic scaffolds for hard tissue engineering applications. Mater. Sci. Eng. C 71, 431–438.

Saito, T., Uchida, I., Takeda, M., 2002. Skeletal growth of the deep-sea hexactinellid sponge Euplectella oweni, and host selection by the symbiotic shrimp Spongicola japonica (Crustacea: Decapoda: Spongicolidae). J. Zool. 258, 521–529.

Sarikaya, M., Fong, H., Sunderland, N., Flinn, B.D., Mayer, G., Mescher, A., Gaino, E., 2001. Biomimetic model of a sponge-spicular optical fiber—mechanical properties and structure. J. Mater. Res. 16, 1420–1428.

Subhash, G., Ridgeway, S., 2022. Mechanics of Materials Laboratory Course. Springer Nature.

Sun, J., Bhushan, B., 2012. Hierarchical structure and mechanical properties of nacre: a review. RSC Adv. 2, 7617–7632.

Tang, Q., Wan, B., Yuan, X., Muscente, A.D., Xiao, S., 2019. Spiculogenesis and biomineralization in early sponge animals. Nat. Commun. 10, 3348.

Tavangarian, F., Sadeghzade, S., Davami, K., 2021. A novel biomimetic design inspired by nested cylindrical structures of spicules. J. Alloys Compd. 864, 158197.

Uriz, M., Turon, X., Becerro, M.A., Agell, G., 2003. Siliceous spicules and skeleton frameworks in sponges: origin, diversity, ultrastructural patterns, and biological functions. Microsc. Res. Tech. 62, 279–299. https://doi.org/10.1002/jemt.10395.

Wang, J., Goyanes, A., Gaisford, S., Basit, A.W., 2016. Stereolithographic (SLA) 3D printing of oral modified-release dosage forms. Int. J. Pharm. 503, 207–212.

Wang, X., Wiens, M., Schloßmacher, U., Jochum, K.P., Schröder, H.C., Müller, W.E.G., 2012. Bio-sintering/Bio-fusion of silica in sponge spicules. Adv. Eng. Mater. 14 https://doi.org/10.1002/adem.201180059.

Wei, J., Pan, F., Ping, H., Yang, K., Wang, Y., Wang, Q., Fu, Z., 2023. Bioinspired additive manufacturing of hierarchical materials: from biostructures to functions. Research 6, 164. https://doi.org/10.34133/research.0164.

Yancey, R.N., 2016. Challenges, opportunities, and perspectives on lightweight composite structures: aerospace versus automotive. Lightweight Composite Structures in Transport, pp. 35–52.

Yang, Y., Li, X., Chu, M., Sun, H., Jin, J., Yu, K., Wang, Q., Zhou, Q., Chen, Y., 2019. Electrically assisted 3D printing of nacre-inspired structures with self-sensing capability. Sci. Adv. 5, eaau9490 https://doi.org/10.1126/sciadv.aau9490.

Yang, Z., Xue, J., Li, T., Zhai, D., Yu, X., Huan, Z., Wu, C., 2022. 3D printing of sponge spicules-inspired flexible bioceramic-based scaffolds. Biofabrication 14, 035009. https://doi.org/10.1088/1758-5090/ac66ff.

Zhao, H., Liu, S., Wei, Y., Yue, Y., Gao, M., Li, Y., Zeng, X., Deng, X., Kotov, N.A., Guo, L., Jiang, L., 2022a. Multiscale engineered artificial tooth enamel. Science 375, 551–556. https://doi.org/10.1126/science.abj3343.

Zhao, H., Liu, S., Yang, X., Guo, L., 2022b. Role of inorganic amorphous constituents in highly mineralized biomaterials and their imitations. ACS Nano 16, 17486–17496. https://doi.org/10.1021/acsnano.2c05262.

Zhao, H., Yang, Z., Guo, L., 2018. Nacre-inspired composites with different macroscopic dimensions: strategies for improved mechanical performance and applications. NPG Asia Mater. 10, 1–22.

Zhou, Y., Liu, K., Zhang, H., 2023. Biomimetic mineralization: from microscopic to macroscopic materials and their biomedical applications. ACS Appl. Bio Mater. 6, 3516–3531. https://doi.org/10.1021/acsabm.3c00109.